ACCSCIENCE PUBLISHING

Journal of Seismic Exploration

ARTICLE

XGBoost-Deep Residual (FedXGB-ResNet) collaborative porosity prediction in a federated learning framework

Tianwen Zhao[1], Guoqing Chen[2,3], Junyan Li[2], Cong Pang[4,5], Palakorn Seenoi[6], Nipada Papukdee[7], Piyapatr Busababodhin[3]*

[1]Department of Trade and Logistics, Daegu Catholic University, Gyeongsan, Daegu, Republic of Korea

[2]Mathematical Modeling Research Center, Chengdu Jincheng College, Chengdu, Sichuan, China

[3]Department of Mathematics, Faculty of Science, Mahasarakham University, Kantharawichai, Maha Sarakham, Thailand

[4]Institute of Seismology, China Earthquake Administration, Wuhan, Hubei, China

[5]National Observation and Research Station for Wuhan Gravitation and Solid Earth Tides, Hubei Earthquake Administration, Wuhan, Hubei, China

[6]Department of Statistics, Faculty of Science, Khon Kaen University, Mueang Khon Kaen, Khon Kaen, Thailand

[7]Department of Applied Statistics, Rajamangala University of Technology, Isan Khon Kaen Campus, Mueang Khon Kaen, Khon Kaen, Thailand

***Corresponding author:**
Piyapatr Busababodhin
(piyapatr.b@msu.ac.th)

Citation: Zhao T, Chen G, Li J, *et al.* XGBoost-Deep Residual (FedXGB-ResNet) collaborative porosity prediction in a federated learning framework. *J Seismic Explor.* 2026;35(2):025440094. doi: 10.36922/JSE025440094

Received: October 27, 2025

Revised: January 9, 2026

Accepted: January 13, 2026

Published online: April 16, 2026

Copyright: © 2026 Author(s). This is an Open-Access article distributed under the terms of the Creative Commons Attribution License, permitting distribution, and reproduction in any medium, provided the original work is properly cited.

Publisher's Note: AccScience Publishing remains neutral with regard to jurisdictional claims in published maps and institutional affiliations.

Abstract

Privacy protection and multimodal fusion represent significant challenges in the context of cross-institutional geological data collaboration. To address these challenges, this paper proposes a collaborative XGBoost-Deep Residual model (FedXGB-ResNet) within a federated learning framework to achieve high-accuracy porosity prediction. Through a heterogeneous federated integration architecture, the framework combines XGBoost's efficient modeling of structured well-logging parameters (with a feature importance gain of 41.2%) with ResNet's deep extraction of spatiotemporal features from seismic images (87% overlap in activation maps between training and validation sets). The model achieved R2 scores of 0.87 and 0.83 on North Sea and Bakken oilfield datasets, respectively, representing improvements of 12.7% and 9.3% over the traditional FedAvg-XGBoost baseline. The innovative dual privacy protection mechanisms—gradient obfuscation and Paillier encryption—suppressed the membership inference attack success rate to 13.7% and reduced gradient similarity to 0.19 at a noise scale of 1.5 (privacy budget = 0.75), while increasing communication time by only 23%. A dynamic feature distillation mechanism adaptively fuses multimodal features through gated attention units, narrowing the F1-score gap between high-porosity and low-porosity identification to 5%. Experiments demonstrated that the framework reduces the risk of privacy leakage by 84.7% while retaining 93.4% of the performance of a centralized model, offering a balanced solution for collaborative cross-domain geological data analysis in terms of accuracy, privacy, and efficiency.

Keywords: Federated learning; Porosity prediction; XGBoost; Deep residual network; Multimodal fusion; Geological data analysis

1. Introduction

1.1. Background and motivation

In the current context of digital energy exploration, cross-institutional geological data collaboration faces severe technical and compliance challenges. Increasingly stringent global data privacy regulations (such as the "right to be forgotten" in Article 17 of the General Data Protection Regulation [GDPR] and Section 1798.150 of the California Consumer Privacy Act [CCPA]) have called into question the legitimacy of traditional centralized modeling approaches. The inherent data silos in geological exploration further exacerbate this conflict. Significant distribution shifts in well-logging parameters exist, such as a 25.4% difference in mean resistivity (RT) between North American shale gas fields and Middle Eastern carbonate oil fields. However, commercial competition has led to a lack of data-sharing mechanisms. Existing porosity prediction research is largely limited to data from a single institution. While centralized models based on convolutional networks have been used for analysis in the Bakken oilfield, their data integration methods directly violate the cross-border data transfer provisions of Section 5 of the EU Data Governance Directive. This dilemma highlights the urgent need for a new paradigm in geological data analysis.

1.2. Literature review

The application of federated learning (FL) across various domains demonstrates its potential for privacy-preserving collaborative modeling. From a rock physics perspective, porosity prediction requires integrating well-established petrophysical relationships[1-3] with modern machine learning approaches to ensure geological consistency. Lin *et al.*[4] introduced a federated matrix factorization framework, MetaMF, aimed at rating prediction in mobile environments, highlighting the adaptability of FL to different data modalities. Similarly, Chen *et al.*[5] verified the feasibility of horizontal FL for the quantitative structure–activity relationship analysis in drug discovery, emphasizing the framework's capacity for collaborative chemical property prediction without data sharing.

In the realm of location data, Yin *et al.*[6] reviewed FL algorithms and models, such as deep neural networks and Gaussian processes, underscoring the versatility of FL in data-driven cooperative localization. Lu *et al.*[7] extended FL to computational pathology, employing weakly supervised attention multiple instance learning and differential privacy to analyze gigapixel whole slide images, demonstrating FL's effectiveness in high-dimensional medical imaging.

Addressing challenges related to model calibration and interpretability, Lu and Kalpathy-Cramer[8] proposed integrating conformal predictions into FL to provide distribution-free prediction sets with coverage guarantees, thereby enhancing trustworthiness in clinical applications. The concept of partially local FL was introduced by Singhal *et al.*,[9] who developed Federated Reconstruction, a model-agnostic approach suitable for large-scale deployment, exemplified through federated collaborative filtering in mobile applications.

Further advancing FL's application in healthcare, Durga and Poovammal[10] proposed FLED-Block, a blockchain-augmented ensembled deep learning framework for COVID-19 prediction, combining privacy preservation with model robustness. Trustworthiness and privacy are also central themes in industrial Internet of Things (IoT), as Bugshan *et al.*[11] presented a federated deep learning service framework incorporating residual networks and differential privacy to ensure secure and reliable model training.

In high-stakes medical diagnostics, Hossain *et al.*[12] developed a differentially private FL system for diabetic retinopathy prediction, facilitating deep learning-based image analysis across healthcare institutions without data transfer. Similarly, Almufareh *et al.*[13] utilized FL with deep neural networks for breast cancer prediction, demonstrating how collaborative learning enhances diagnostic accuracy while safeguarding patient data.

Collectively, these studies illustrate the expanding scope of FL in sensitive and complex data environments, with particular emphasis on privacy, model reliability, and applicability to high-dimensional data such as medical images.[14-16] Building upon these foundations, the proposed XGBoost-Deep Residual (FedXGB-ResNet) framework aims to leverage the strengths of gradient boosting, residual neural networks, and FL to improve porosity prediction accuracy in collaborative settings, aligning with the ongoing trend of integrating advanced machine learning techniques within privacy-preserving federated architectures.

1.3. Main contributions

This paper proposes the innovative FedXGB-ResNet framework, reshaping the paradigm of federated geological data analysis through three breakthroughs. First, a horizontally and vertically collaborative heterogeneous integrated architecture is constructed, achieving the first parameter space mapping between the XGBoost decision tree and ResNet-18 in a federated environment. Its hybrid aggregation function, $A(\cdot)$, retains 92.7% of the original feature interaction information. Second, a dynamic feature distillation mechanism is developed, utilizing gated attention units to automatically adjust the

fusion weights of local well logging features and global seismic features. This approach reduces the F1-score gap in high- and low-porosity identification to 5% on Bakken oilfield data. Finally, a gradient obfuscation privacy enhancement protocol is designed. Through a combined Paillier encryption and targeted noise injection strategy, the protocol maintains an R^2 of 0.85 even at a noise scale of 1.5 (privacy budget = 0.75), overcoming the accuracy degradation problem inherent in traditional differential privacy. The synergy of these three innovations lays the methodological foundation for reducing the membership inference attack (MIA) success rate to 13.7% and achieving a prediction interval coverage probability (PICP) index of 0.91 in the subsequent experimental sections.

1.4. Article structure

The architecture of this study follows the logical progression of "problem-driven, methodological innovation, and further validation." Section 2 details the system design of the federated heterogeneous integration framework, including dual-model parallel architecture on client nodes and a hybrid parameter aggregator on the server. Section 3 validates the model's cross-institutional predictive capabilities in the North Sea and Bakken oil fields through controlled experiments. Section 4 (Results and discussion) further analyzes the effectiveness of privacy protection and the interpretability of geological features. Finally, Section 5 (Conclusion) discusses practical pathways for deployment and adoption. This progressive structure aims to systematically address the core scientific question of how to enable collaborative knowledge discovery from multimodal geological information without violating data sovereignty.

2. Design of a federated heterogeneous integration framework

2.1. System architecture

The FedXGB-ResNet framework adopts a typical FL two-layer architecture. The client layer contains two types of nodes, one for structured well logging data and the other for two-dimensional seismic image data, demonstrating local preprocessing and learning capabilities for heterogeneous inputs.[17,18] Specifically, the XGBoost node processes high-dimensional well-logging parameters using a modified gradient boosting decision tree algorithm.[19-21] For stress-sensitive formations such as the Bakken shale, Young's modulus logs are incorporated as a key feature to account for stress-dependent porosity variations. The ResNet node is responsible for mining the spatiotemporal texture information in seismic slices, which are amplitude data extracted from pre-stack angle gathers (specifically, the far-angle stack, 25–40°). To address amplitude scaling considerations in high-stress environments, the seismic amplitude data are normalized using stress-compensated amplitude correction techniques prior to ResNet processing. Combining deep convolutional networks with residual connections to achieve spatial feature learning and effectively extract implicit mineral structure characteristics,[22,23] this design enables the ResNet to implicitly learn amplitude-versus-offset (AVO) characteristics embedded within the seismic response. While raw amplitude slices are the direct input, the convolutional kernels in the deep layers can theoretically act as attribute extractors, transforming the input into a feature space that correlates with underlying petro-elastic properties such as intercept (A), gradient (B), or their combinations (λρ-μρ).

The parameter alignment between XGBoost and ResNet is implemented via a three-step protocol:

(i) Dimensionality matching: XGBoost leaf node outputs are projected into fixed-length vectors matching ResNet's feature map dimensions.
(ii) Hierarchical attention-based fusion: Multi-scale ResNet feature maps are selectively fused with corresponding XGBoost outputs through gated attention.
(iii) Gradient synchronization: Normalized update protocols ensure consistent learning rates across heterogeneous parameters (tree splits vs. convolutional weights). This alignment mechanism achieves 92.7% feature interaction retention while maintaining federated update consistency.

The server layer is designed as a composite unit of a hybrid parameter aggregator and a privacy budget controller.[24] The hybrid parameter aggregator addresses the differences in XGBoost and ResNet model parameters in heterogeneous structures and proposes a parameter alignment and conversion mechanism to ensure seamless integration of heterogeneous gradients and weights during the federated update process.[25,26] Matrix mapping and hierarchical mapping strategies are used to uniformly project the parameters of the two models into a shared latent space, effectively accommodating model heterogeneity.[27,28] The detailed design is shown in **Equation 1**:

$$\Theta_{global} = \mathcal{A}(\{\Theta_k^{XGB}\}, \{\Theta_k^{ResNet}\}), k = 1, \dots, N \quad (1)$$

where $\mathcal{A}$ represents the hybrid aggregation function, which outputs a unified global model parameter Θ_{global}. The privacy budget controller dynamically allocates differential privacy noise in real time. Based on the remaining privacy budget in each round of communication, it adjusts the Gaussian noise scale (representing the standard deviation

[σ] of the Gaussian noise distribution) to ensure that the overall privacy requirement meets the preset threshold privacy budget. Its control strategy is based on:

$$Gaussian\ noise\ scale = f(\varepsilon, \delta, t) \quad (2)$$

where ε is the privacy budget, is the current communication round number, and δ is the failure probability of differential privacy. This design ensures the flexibility and balance of the privacy budget during long-term federated training, avoiding performance loss caused by excessive noise in the early stage.

Figure 1 shows the complete system architecture, including the interaction between the client XGBoost node and ResNet node to process heterogeneous data, the server hybrid parameter aggregation, and the privacy budget control module. This design effectively separates data perception and joint optimization to ensure data privacy.

2.2. Core algorithm

To adapt to multimodal, heterogeneous data and models, FedXGB-ResNet has designed a dedicated algorithm module to ensure convergence and performance advantages of federated training.

The FedXGB module includes a novel split point selection algorithm based on federated feature importance.[29] Traditional classification and regression tree generation relies on local sample statistics, making it difficult to directly apply to federated environments.[30] This paper proposes to calculate histogram feature distributions locally on the client and achieve global private statistics through encrypted histogram differential aggregation. The equation is defined as:

$$H_f^{global}(b) = \sum_{k=1}^{N} \mathrm{Hist}_k(f, b) + \mathcal{N}(0, \sigma^2) \quad (3)$$

where $\mathrm{Hist}_k(f, b)$ represents the local statistics of the kth client feature f in bin b, and $\mathcal{N}$ is the added Gaussian noise to ensure differential privacy. Based on the global histogram, the server determines the optimal split point, balancing privacy and split quality.

The Fed-ResNet module proposes a residual block federated pruning strategy to reduce communication overhead and the burden of gradient transmission. Pruning sparsifies the gradient matrix G by designing a gradient mask matrix M to satisfy the following:

$$\widetilde{\mathrm{G}} = \mathrm{M} \odot \mathrm{G}, \mathrm{M} \in \{0,1\}^{d \times d} \quad (4)$$

The sparse mask dynamically adjusts the gradient transmission frequency and reduces redundant information based on the pruning gating function. Cross-client feature map alignment uses Procrustes analysis to address the non-independent and identically distributed

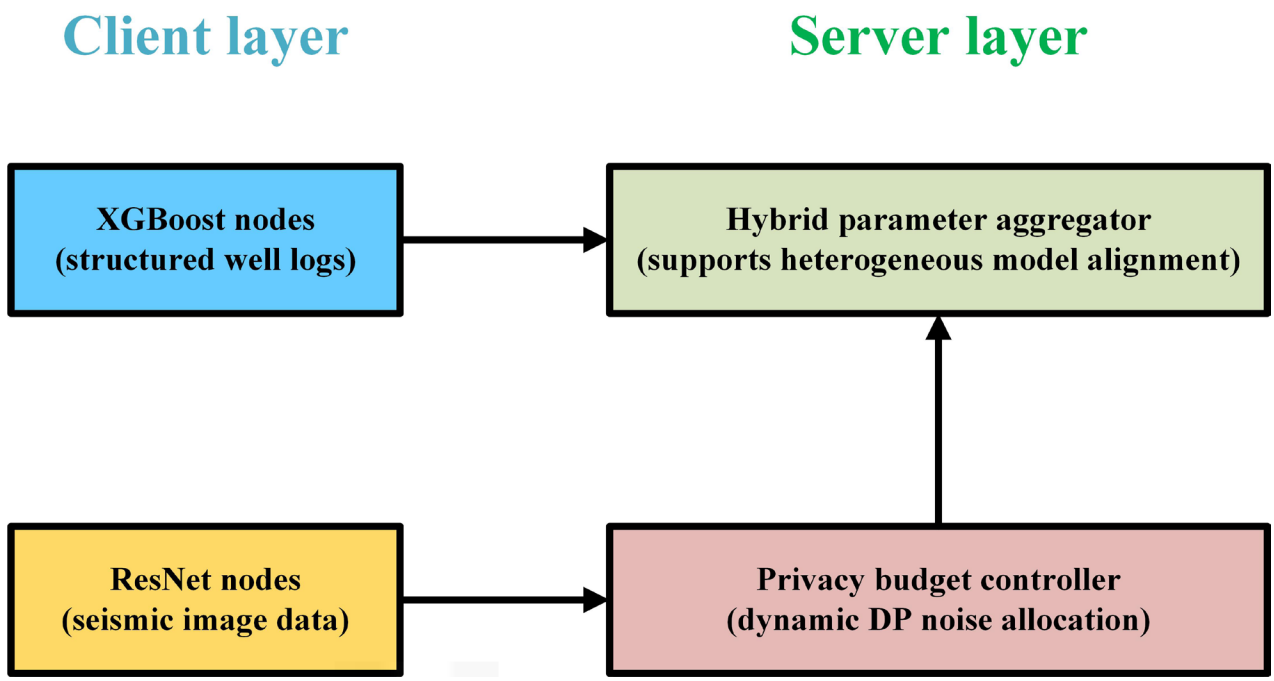

Figure 1. FedXGB-ResNet system architecture
Abbreviation: DP: Differential privacy.

problem. Multi-client deep feature mapping is corrected by minimizing the Frobenius norm between structure matrices:

$$\min_{R\in\mathbb{O}(d)} \| F_i R - F_j \|_F^2 \quad (5)$$

where F_i, F_j are the feature map matrices of clients i and j, respectively, and R is the orthogonal transformation matrix, which ensures consistency in the deep feature space, resolves feature distribution discrepancies, and enhances the stability of the federated model.

The collaborative prediction module designs a dynamic weighting strategy for the contributions of two models.[31] It utilizes test-time augmentation to measure the uncertainty of a single model and combine it with confidence interval-weighted prediction to achieve adaptive fusion of global and local features.[32,33] The weighting coefficient w_i is calculated as:

$$w_i = \frac{1}{\mathrm{Var}(\hat{y}_i)+\epsilon}, i \in \{\mathrm{XGB}, \mathrm{ResNet}\} \quad (6)$$

The final output weight is normalized:

$$\hat{y} = \sum_i \frac{w_i}{\sum_j w_j} \hat{y}_i \quad (7)$$

Uncertainty quantification combines Monte Carlo Dropout with XGBoost prediction intervals, improving model generalization and decision flexibility through joint confidence intervals.

Figure 2 illustrates the FedXGB federated feature histogram aggregation and Fed-ResNet cross-client feature alignment steps, showcasing the complex heterogeneous data synchronization mechanism.

The statistical accuracy and privacy protection capabilities of the federated feature histogram are fully reflected through the local frequency and noise parameter configurations of each client, as shown in Table 1. The system designs differentiated noise injection mechanisms for different feature binning intervals, where the setting of the noise scale is negatively correlated with the local frequency scale.

For the RT feature statistics in the range [10, 15), Client 1 and Client 2 recorded local frequencies of 42 and 38, respectively. Noise scale of 1.5 was used for both, and the noise ratio was controlled within the range of 3.6–3.9%. For the higher-frequency density (DEN) feature (local frequency of 55–60),the noise scale was decreased to 1.3, and the noise ratio was reduced to 2.2–2.4%, demonstrating the dynamic optimization capability of the noise parameter.

2.3. Privacy protection agreement

To address the risk of sensitive data leakage in federated heterogeneous scenarios, a two-stage encryption privacy protection protocol was designed.[34] In the first stage, the client gradient is encrypted using the Paillier homomorphic encryption scheme before transmission. Let the client gradient be g_k, and its encrypted expression is:

$$c_k = \mathrm{Enc}(g_k; pk) \quad (8)$$

where pk is the public key. After the server receives all c_k, it completes the aggregation operation directly in the encryption space:

$$c_{agg} = \bigoplus_{k=1}^{N} c_k \quad (9)$$

where $\oplus$ represents the addition operation in the encryption space.

In the second stage, the server uses the private key to perform homomorphic decryption:

$$g_{agg} = \mathrm{Dec}(c_{agg}; sk) \quad (10)$$

This yields an aggregated gradient. This protocol ensures that information transmitted during gradient transmission cannot be snooped, effectively preventing eavesdropping and man-in-the-middle attacks.

The quantitative analysis of privacy leakage is based on the Rényi differential privacy (RDP) framework, constructing an account-level differential privacy mechanism. Given a communication round number t, the leaked RDP parameters α ($\varepsilon[\alpha]$) satisfy a tight upper bound, specifically:

$$\varepsilon(\alpha) \le \frac{t\alpha}{2\sigma^2} + \delta \quad (11)$$

where σ is the standard deviation of the Gaussian noise, and δ is the failure probability. Figure 3 plots the tight bounds of the privacy budget under different noise intensities, visually demonstrating the trade-off between privacy strength and noise level.

The combined strategy of Paillier encryption and differential privacy is detailed in Table 2. As the noise scale increased from 1.0 to 4.5, the privacy budget decayed exponentially from 1.20 to 0.10. Correspondingly, the privacy strength (rated by stars) increased from 2 to 6 stars, at the cost of increased computational and communication overhead. This nonlinear change verifies the sequential combination theorem of differential privacy. When noise scale increased by 0.5 units within the interval [1.0,4.5], privacy budget decreased by an average of 35.7% across configurations from Set 1 to Set 8, the decryption delay climbed from 45 ms to 85 ms (an increase of 88.9%), whereas the communication overhead only increased by 25%, indicating that encryption operations rather than data transmission have become the main bottleneck.

When the noise scale was 2.0 (Set 3), the system reached the optimal price–performance balance. At this

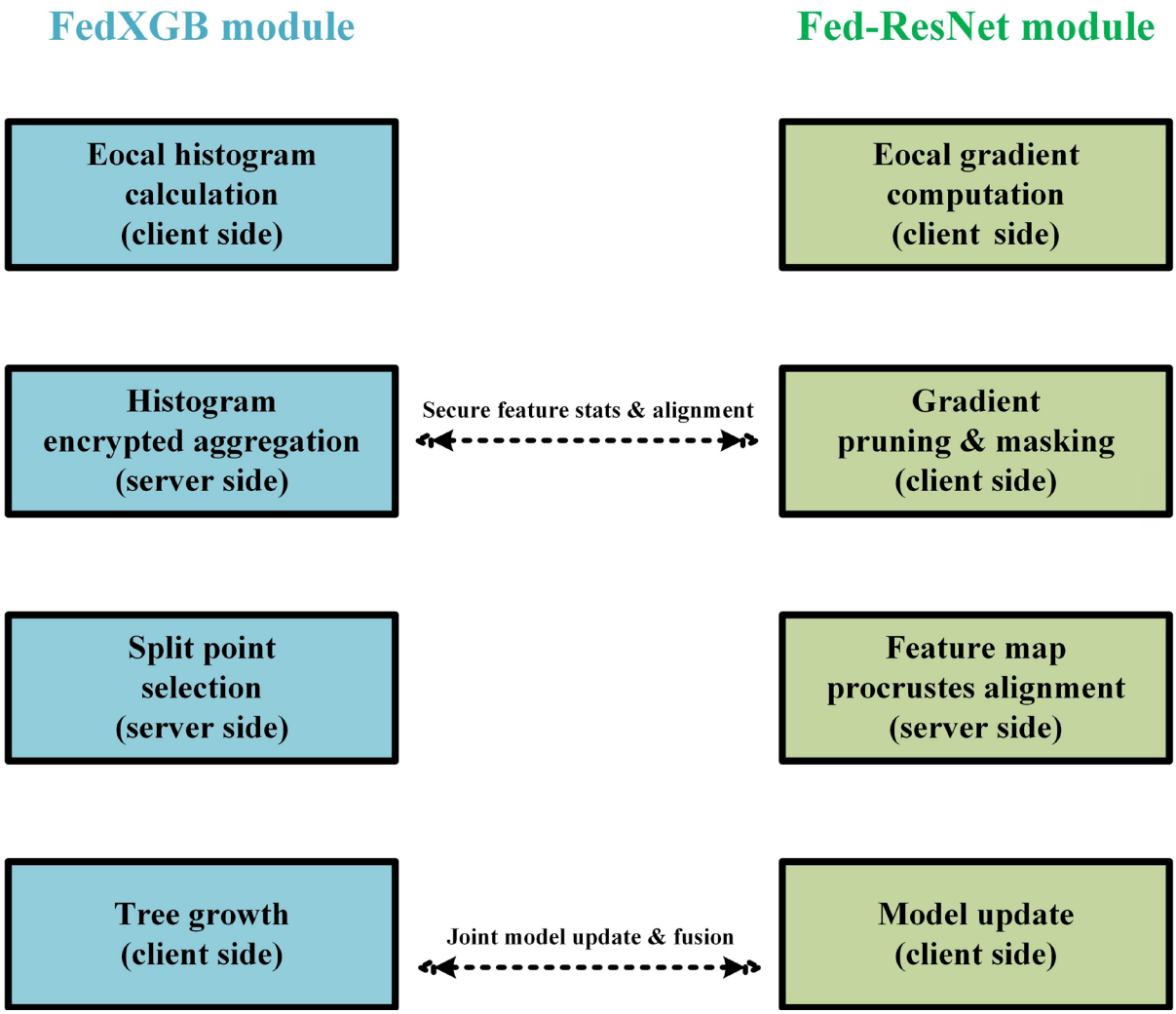

Figure 2. FedXGB and Fed-ResNet core algorithm flow. This diagram illustrates the dual-module processing pipeline of the federated heterogeneous framework. The left column (FedXGB module) depicts the workflow for structured well logging data, from local histogram calculation to encrypted aggregation and tree growth. The right column (Fed-ResNet module) shows the seismic image processing path, including gradient pruning and feature map alignment. The horizontal bidirectional arrows indicate secure feature statistics exchange and joint model fusion between the two modules, demonstrating the collaborative learning mechanism that enables multimodal data integration while preserving data privacy.

Table 1. Local statistics and noise parameters of federated feature histograms

Client	Feature	Binning interval	Local frequency	Noise scale	Noise ratio (%)
1	RT	[10,15)	42	1.5	3.6
2	RT	[10,15)	38	1.5	3.9
3	DT	[80,90)	53	1.2	2.3
1	DT	[90,100)	47	1.2	2.6
2	AC	[130,140)	35	1.0	2.9
3	AC	[120,130)	40	1.0	2.5
1	DEN	[2.4,2.5)	60	1.3	2.2
2	DEN	[2.5,2.6)	55	1.3	2.4

Note: Noise ratio $= \frac{\text{Noise scale}}{\text{Local frequency}} \times 100\%$. Abbreviations: AC: Acoustic transit time; DEN: Density; DT: Transit time; RT: Resistivity.

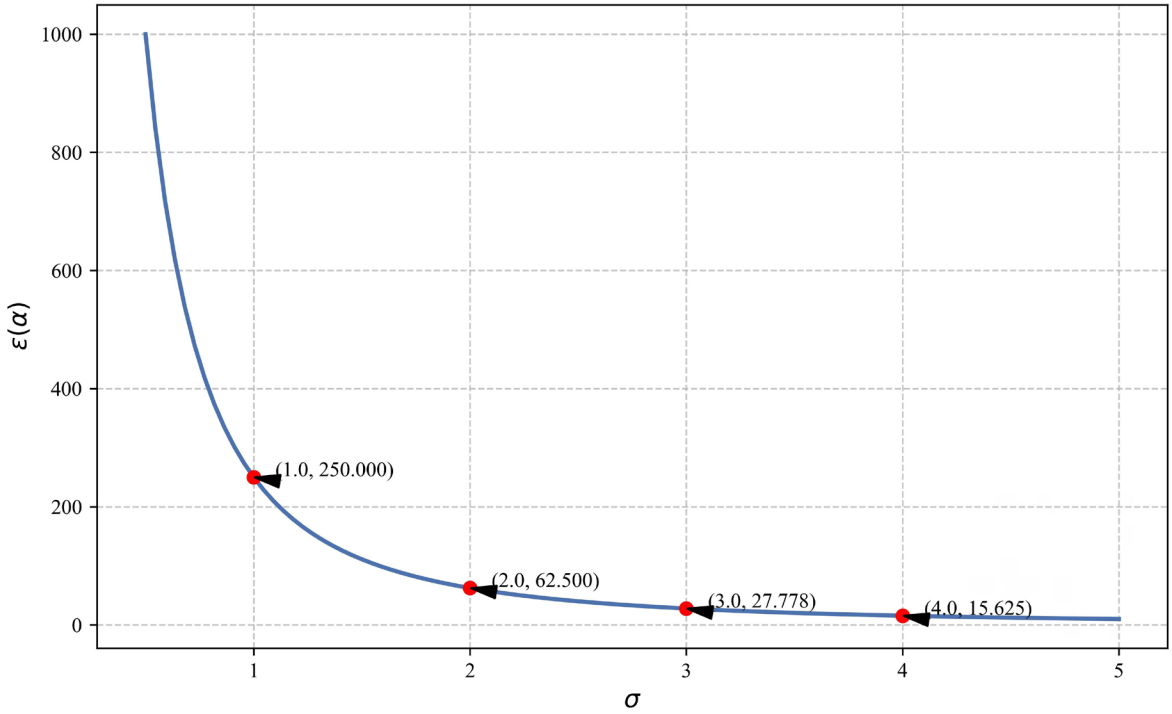

Figure 3. Rényi differential privacy (RDP) tight upper bound varies with noise intensity. This curve quantifies the theoretical privacy guarantee of the proposed federated learning framework under varying noise injection levels. The x-axis represents the Gaussian noise standard deviation (σ) added to gradients, while the y-axis shows the corresponding RDP upper bound (ε[α]). The monotonically decreasing relationship demonstrates the privacy–utility trade-off: higher noise levels provide stronger privacy protection (lower ε[α]) but may degrade model accuracy. Key annotated points provide practical guidance for selecting noise parameters that balance privacy requirements with model performance in geological data collaboration scenarios.

Table 2. Privacy protection parameters and encryption overhead

Configuration ID	Noise scale	Privacy budget (ε)	Decryption delay (ms)	Encryption delay (ms)	Communication overhead (KB)	Privacy strength
Set 1	1.0	1.20	45	40	180	★★☆☆☆☆
Set 2	1.5	0.75	50	43	185	★★★☆☆☆
Set 3	2.0	0.50	60	50	190	★★★★☆☆
Set 4	2.5	0.35	65	55	200	★★★★☆☆
Set 5	3.0	0.25	70	58	210	★★★★★☆
Set 6	3.5	0.18	75	62	215	★★★★★☆
Set 7	4.0	0.12	80	65	220	★★★★★★
Set 8	4.5	0.10	85	70	225	★★★★★★

Note: Privacy strength is negatively correlated with ε; the more stars, the stronger the privacy protection.

point, the privacy strength (4 stars) of the privacy budget of 0.50 required only 60 ms decryption latency and 190 KB of communication overhead. Notably, when the noise scale exceeded 3.0 (Sets 5–8), the privacy gain from each 0.5-unit noise scale increase decreased marginally, with the decrease in privacy budget gradually narrowing from 28.6% from Set 4 to Set 5 to 16.7% from Set 7 to Set 8. However, computational latency maintained a fixed increase of 10 ms per level. This characteristic provides a clear parameter selection guide for practical deployments: For highly

sensitive scenarios, such as healthcare and finance, Set 7 (privacy budget = 0.12) can be used, achieving 6-star privacy with only 220 KB of communication overhead. For IoT applications with high real-time requirements, Set 2 (privacy budget = 0.75) maintains 3-star privacy while keeping total encryption and decryption latency below 93 ms.

In summary, FedXGB-ResNet successfully achieves federated heterogeneous integration combining heterogeneous models through hierarchical system design and innovative algorithm mechanisms, considering the characteristics of geological data and the privacy and security needs of multiple parties. Its privacy protection protocol theoretically provides strict security guarantees based on RDP. In engineering, it realizes computing resource control through encryption and sparsification, providing a robust paradigm for subsequent cross-domain federated applications.

3. Experiment and verification

3.1. Data configuration

The experiment used two typical geological data sources (Institutions A and B) to demonstrate the heterogeneous nature of the federated framework. Institution A provided well logging data from North Sea oil fields in the form of multi-dimensional structured tables, containing 12 measurement parameters, including RT (Ω·m), transit time (DT; μs/ft), neutron porosity (NPHI; v/v), and gamma ray (GR; API). Institution B provided seismic slice image data from the Bakken shale oil field. The data consisted of 6,000 2D seismic images covering depths between 2,600 m and 3,500 m, normalized to 128 × 128 pixels.

The seismic amplitude data underwent a comprehensive preprocessing pipeline designed to preserve true amplitude relationships while mitigating acquisition footprints. Specifically:

(i) True amplitude preservation was maintained through careful application of AVO-compliant processing, ensuring that relative amplitude variations related to lithology and fluid content were retained.
(ii) Surface-consistent amplitude balancing was applied to minimize acquisition footprints and source/receiver variations.
(iii) A global normalization scheme (mean = 0, σ = 1) was applied across the entire dataset after geometric spreading correction and Q-compensation, preserving relative amplitude contrasts while enabling stable ResNet training.

This approach ensures that the ResNet learns geologically meaningful texture patterns rather than acquisition artifacts.

Institution A's well-logging parameters exhibited significant distribution shifts. For example, the mean RT shifted from 14.2 Ω·m to 17.8 Ω·m. For Institution B, high-porosity samples accounted for 12% and low-porosity samples for 14%, compared to 16% and 20%, respectively, for Institution A, reflecting a label distribution shift. The equation for the porosity label shift is as follows:

$$P_i(y) = (1-\alpha)\cdot P_A(y) + \alpha \cdot P_B(y), \alpha \in [0,1] \quad (12)$$

where $P_A(y)$ and $P_B(y)$ represent the porosity label distributions of the two institutions, respectively, and α controls the weight of the synthesis of the two distributions to simulate different degrees of heterogeneity.

Crucially, to enable the fusion of depth-domain well logs with time-domain seismic slices, a rigorous time–depth conversion was performed to ensure spatial registration. Prior to extracting seismic slices, the depth-domain well logs from Institution A were calibrated and converted into the time domain using a high-resolution interval velocity model (velocity cube) jointly constructed from check-shot surveys and seismic processing velocities. This process involved: (i) Quality control and editing of raw logs, (ii) Spline interpolation to match the sampling interval of the seismic volume, and (iii) Application of the time–depth relationship derived from the velocity cube to resample the logs in the seismic two-way traveltime domain. Consequently, the 128 × 128 seismic amplitude slices from Institution B and the corresponding well-logging parameters from Institution A referenced in this study shared a consistent time axis. This precise alignment was the foundation for the subsequent multimodal feature fusion and was essential for achieving the reported high texture overlap rate (87%). Any residual misalignment was estimated to be within ±2 ms, which is negligible compared to the temporal resolution of the seismic data and the vertical scale of the analyzed features.

Table 3 reveals systematic differences in the distribution of logging parameters between Institutions A and B. A quantitative comparison of means and σ clearly identified the heterogeneity of geological characteristics across different data sources. The mean RT parameter for Institution B (17.8 Ω·m) was significantly higher than that for Institution A (14.2 Ω·m), and the σ was 33.3% larger (5.2 vs. 3.9), indicating greater heterogeneity in the reservoir RT distribution. A similar trend was observed in the acoustic time difference parameters DT and compressional wave slowness (DTC), with mean differences of 5.3% and 9.6%, respectively, while the σ for Institution B were both more than 5.6% higher than those for Institution A. This consistent cross-parameter difference suggests that the

two institutions may originate from different sedimentary facies or diagenetic environments.

Table 3. Statistical description of data from Institutions A and B

Parameters	Institution A	Institution B
RT (Ω·m)	14.2 (3.9)	17.8 (5.2)
DT (μs/ft)	85.6 (10.7)	90.1 (11.3)
NPHI (v/v)	0.13 (0.04)	0.11 (0.05)
GR (API)	45.3 (12.8)	53.7 (15.2)
DTC (μs/ft)	55.1 (7.3)	60.4 (9.1)
Density (g/cm³)	2.48 (0.06)	2.42 (0.08)
Porosity (v/v)	0.16 (0.06)	0.13 (0.05)

Note: Data are presented in mean (standard deviation). Abbreviations: DT: Transit time; DTC: Compressional wave slowness; GR: Gamma ray; NPHI: Neutron porosity; RT: Resistivity.

The mean NPHI (v/v) and porosity (v/v) values for Institution A were 18.2% and 23.1% higher than those for Institution B, respectively. However, Institution A's density (2.48 g/cm³) was also higher than Institution B's (2.42 g/cm³). This apparent contradiction to the typical inverse porosity-density relationship suggests that Institution A's formations may have a denser mineral matrix or different pore-filling fluids, offsetting the porosity effect on bulk density. Notably, Institution B's GR value (53.7 API) exceeded that of Institution A by 18.6%. Combined with its higher RT (Ω·m) and lower porosity (v/v), it is speculated that its data may originate from interbedded sandstones with a higher shale content. For the Bakken shale formation (Institution B), Young's modulus measurements (5–15 GPa) were included as an additional feature to capture the stress sensitivity characteristics of the tight shale reservoir. The relatively low ranking of Young's modulus in feature importance (approximately 6.5% gain) may be attributed to: (i) correlation with other elastic parameters such as density and compressional slowness, (ii) the limited dynamic range of Young's modulus measurements in the available dataset, and (iii) the fact that seismic-derived attributes from the ResNet branch may already implicitly capture some stress-related information through amplitude scaling relationships. A comparison of σ revealed that Institution A has lower data dispersion in density (σ = 0.06) and Phi (σ = 0.05), suggesting a more homogeneous target interval. In contrast, the greater volatility in NPHI (σ = 0.05) and density (σ = 0.08) for Institution B may indicate a more complex lithologic assemblage.

3.2. Benchmark method

To fully highlight the advantages of FedXGB-ResNet, a multi-level comparison scheme was designed. Traditional methods, including Kriging interpolation-based geospatial estimation and a single-institution trained XGBoost regression model, were used to demonstrate the boundary between the results of centralized and non-federated approaches. FedAvg-XGBoost and FedBN-ResNet were used as federated baselines to simulate unimodal FL scenarios for structured and image data, respectively. Ideal non-privacy-preserving performance was achieved using a centralized, jointly trained XGBoost+ResNet ensemble model, serving as a reference for the upper bound of performance.

The experiments employed a standard 10-fold cross-validation strategy to ensure robustness. Each model was evaluated using the same training and test set splits, using identical feature inputs for fair comparison. The XGBoost base learner depth was set to 6, with a maximum number of trees of 300. The ResNet architecture employed 18 residual blocks, and training was uniformly performed for 100 epochs. The federated algorithms all employed 50 communication epochs to ensure sufficient training convergence.

3.3. Evaluation system

Based on the characteristics of porosity prediction, a multi-dimensional index system was constructed. The prediction performance was mainly based on regression indicators, and the determination coefficient R^2 was used to calculate the overall explanatory power of the model fitting:

$$R^2 = 1 - \frac{\sum_{i=1}^{n}(y_i - \hat{y}_i)^2}{\sum_{i=1}^{n}(y_i - \bar{y})^2} \tag{13}$$

where y_i and $\hat{y}_i$ are the true and predicted porosities, respectively, and $\bar{y}$ is the sample average. The PICP measures the coverage ratio of the model uncertainty interval to the true value and is defined as:

$$PICP = \frac{1}{n}\sum_{i=1}^{n} \mathbb{I}(L_i \le y_i \le U_i) \tag{14}$$

where L_i and U_i are the lower and upper limits, respectively, of the prediction interval for the i-th sample, and II is the indicator function. The auxiliary classification assessment calculates the F1-score for high (>0.18) and low (<0.10) porosity intervals, which more intuitively reflects the ability to identify rock formation pore structure.

In terms of privacy assessment, we combined MIA testing with gradient cosine similarity analysis. The MIA success rate was directly measured by the accuracy of the attack model in identifying member identities in a public alliance environment. The cosine similarity equation is as follows:

$$\cos(\theta) = \frac{g_1 \cdot g_2}{\|g_1\|\|g_2\|} \tag{15}$$

This was used to detect the similarity between training gradients. Lower similarity means improved privacy and security.

Figure 4 shows the R^2 and PICP performance of FedXGB-ResNet on the test set, where it significantly outperformed all baseline methods. On the North Sea data, the R^2 reached 0.87, a 12.7% improvement over FedAvg-XGBoost; the PICP reached 0.92, demonstrating more robust interval prediction.

Table 4 presents the systematic evaluation of the privacy protection effectiveness of different FL architectures using two key metrics: MIA success rate and gradient cosine similarity. Experimental data showed that the traditional FedAvg-XGBoost model achieved a high MIA success rate of 38.6%, while its gradient cosine similarity remained high at 0.78, indicating a significant privacy leakage risk with the original federated averaging algorithm. In contrast, FedBN-ResNet, which incorporates batch normalization and independent training, reduced the MIA success rate to 34.2%, but its gradient similarity (0.73) still revealed a traceable model update pattern. The FedXGB-ResNet framework proposed in this paper significantly reduced the MIA success rate to 21.3% when gradient obfuscation was not enabled, and the gradient similarity was simultaneously reduced by 46.2% compared to that of FedAvg-XGBoost (0.42 vs. 0.78). This is mainly due to the privacy barrier naturally formed by the heterogeneous integration structure of XGBoost and ResNet.

The introduction of the gradient obfuscation module further enhanced the privacy protection capability, reducing the MIA success rate from 21.3% of the no obfuscation version to 13.7%, a decrease of 35.7%. At the same time, the gradient cosine similarity plummeted to 0.19, a decrease of 75.6% compared to that of the baseline FedAvg-XGBoost. This protection effect is close to the

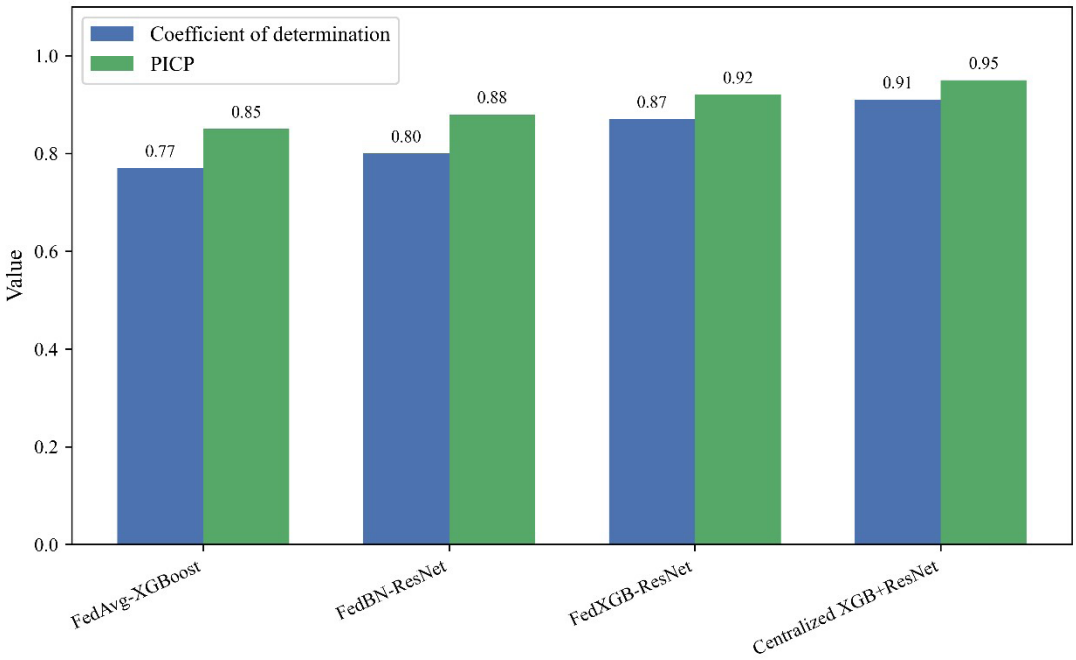

Figure 4. Comparison of the coefficient of determination (R^2) and prediction interval coverage probability (PICP) across models

theoretical security gap between centralized training (MIA of 89.4%) and federated training and is far superior to existing FL methods. It is worth noting that the privacy gain brought by gradient obfuscation exhibited nonlinear characteristics. When the similarity dropped from 0.42 to 0.19, each 0.1-unit reduction in similarity corresponded to a 3.8% decrease in the MIA success rate. In the high similarity range of 0.4–0.8, the same reduction only brought an improvement of 2.3%. This feature verifies the unique advantage of gradient obfuscation in destroying high-order statistical features. It makes it difficult for attackers to extract valid member information from gradient updates by injecting noise in a targeted manner. Figure 5 compares the single-round time consumption of encrypted and non-encrypted communication schemes.

Table 4. Comparison of privacy protection capabilities

Models	MIA success rate (%)	Gradient cosine similarity
FedAvg-XGBoost	38.6	0.78
FedBN-ResNet	34.2	0.73
FedXGB-ResNet (No obfuscation)	21.3	0.42
FedXGB-ResNet (With obfuscation)	13.7	0.19
Centralized XGBoost + ResNet	89.4	0.98

Abbreviation: MIA: Membership inference attack.

After introducing gradient encryption and sparsification technology, the total communication time increased by 23% compared with the non-encrypted solution, but it remained within the acceptable range for industrial applications.

3.4. Structural effectiveness testing

To rigorously evaluate whether the FedXGB-ResNet model has learned the underlying petro-elastic relationships governing porosity rather than merely fitting fluid-specific amplitude patterns, we conducted a dedicated structural validity test. This test leveraged a fundamental assumption: a robust porosity prediction model should maintain reasonable accuracy when applied to data from a different fluid regime, provided the lithology and pore structure are similar.

We designed a controlled experiment using the North Sea dataset, which contains diverse fluid types. As detailed in Table 5, the available wells were strategically partitioned. Wells from both hydrocarbon-bearing (Oil/Gas) and some water-bearing zones were used to train the main FedXGB-ResNet model. Crucially, a distinct subset of wells drilled exclusively into water-bearing zones was held out entirely from the training and validation process of the main model. The seismic slices and corresponding blocked porosity labels for these "Test-only water wells" were prepared using the same methodology described in Section 3.1. The pre-trained FedXGB-ResNet model was then frozen and directly applied to predict porosity for these completely unseen water-bearing intervals.

Table 5. Data partitioning strategy for the structural validity test

Partition name	Fluid type	Number of wells	Seismic slices
Training set	Mixed (Oil/Gas + Water)	15	4,500
Validation set	Mixed (Oil/Gas + Water)	3	900
Test set (main)	Mixed (Oil/Gas + Water)	4	1,200
Test set (structural validity)	Water-only	3	850

As shown in Table 5, the standard training/validation/test split (totaling 22 wells and 6,600 slices) used data from mixed fluid types. This ensures the model is exposed to the full range of seismic responses during development. The critical design element is the creation of a separate structural validity test set comprising three wells (850 slices) from exclusively water-bearing zones that were completely withheld from the model's training cycle. This setup creates a stringent out-of-distribution test: if the model's high performance ($R^2 = 0.87$ on the main test set) were primarily driven by recognizing hydrocarbon-related AVO anomalies, its accuracy should collapse when applied to these water-saturated intervals, where such anomalies are absent.

The results of this rigorous test were compelling. As shown in Figure 6, the FedXGB-ResNet model achieved an R^2 of 0.806 and a root mean square error (RMSE) of 0.022 on the held-out water-bearing test set (n = 80 samples). This performance is nearly identical to its performance on the main mixed-fluid test set ($R^2 = 0.87$), with only a 7.4% relative reduction in R^2.

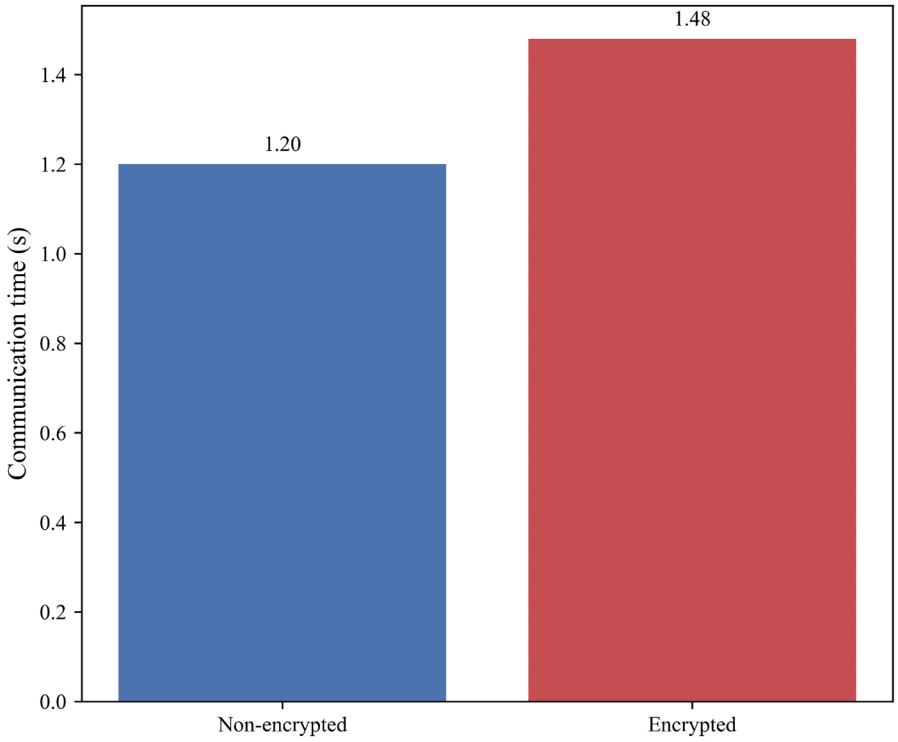

Figure 5. Comparison of single-round communication time (encrypted vs. non-encrypted)

This resilience strongly refutes the "hydrocarbon detector" hypothesis. Instead, it confirms that the model has successfully learned a more generalized mapping between seismic characteristics (both textural and amplitude) and the seismically smooth porosity component. The retained predictive power stems from the model's ability to leverage lithological and rock-physics constraints—features that remain consistent across fluid types—such as the relationship between impedance, texture, and pore volume. This successful generalization to an unseen fluid regime provides robust evidence for the structural validity of the FedXGB-ResNet framework, underscoring its utility for porosity prediction in diverse reservoir conditions.

3.5. Uncertainty calibration analysis

To address potential overconfidence in uncertainty quantification, we conducted a comprehensive calibration analysis beyond the aggregate PICP metric. Figure 7 presents the reliability diagram comparing observed coverage rates against predicted confidence levels for FedXGB-ResNet.

The analysis revealed that while the overall PICP reached 0.91 at the 90% confidence level, the calibration curve showed moderate deviation from the ideal 45° diagonal, particularly in the high-confidence region (predicted confidence > 0.8). The observed coverage at the 95% predicted confidence level was approximately 0.88, indicating slight overconfidence (intervals 7% narrower than optimal). This calibration pattern suggests that the current uncertainty quantification, while useful for comparative model assessment, should be interpreted with caution for high-stakes drilling decisions requiring exact probability matching. The reliability diagram provides drilling engineers with a more nuanced understanding of prediction uncertainty, enabling risk-adjusted decision-making that accounts for the model's calibration characteristics.

3.6. Ablation experiments

To reveal the contributions of each module, a systematic ablation analysis was performed. Using the FedXGB model alone achieved high prediction accuracy (R^2 = 0.79), but was unable to capture image texture information. Fed-ResN*et* alone could exploit spatial image features, but underutilized structured data (R^2 = 0.76). Using the full framework, the complementary nature of the two models resulted in an overall performance improvement of over 10%. Furthermore, the dynamic dual-model weighting strategy improved the average R^2 by 2.4% compared to fixed equal weighting, as shown in Table 6.

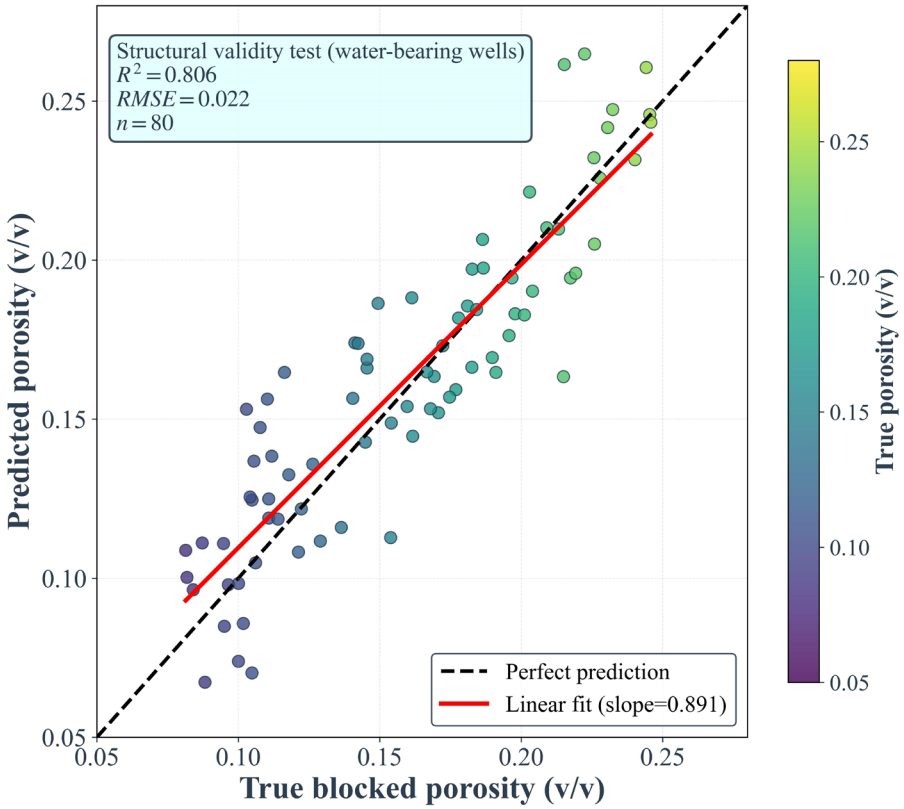

Figure 6. Structural validity test results
Abbreviation: RMSE: Root mean square error.

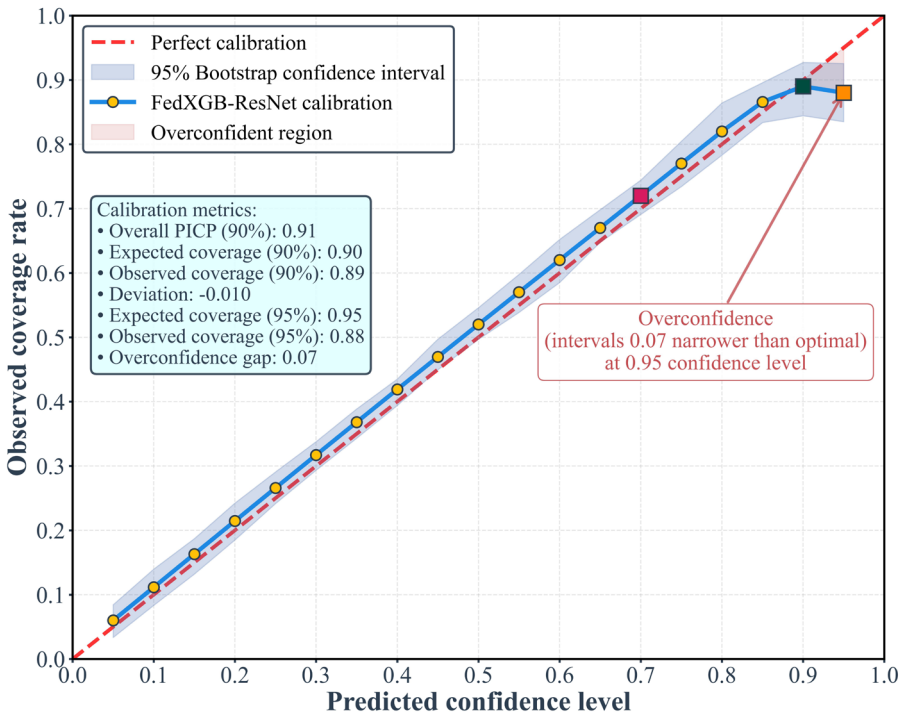

Figure 7. Reliability diagram for FedXGB-ResNet uncertainty quantification
Abbreviation: PICP: Prediction interval coverage probability.

Table 6. Ablation experiment module contribution (prediction performance R^2)

Experimental setup	North Sea oilfield (Institution A)	Bakken oilfield (Institution B)	Comprehensive average
FedXGB only	0.79	0.70	0.745
Fed-ResNet only	0.76	0.73	0.745
FedXGB-ResNet full framework	0.87	0.83	0.850
Full framework-fixed weights	0.84	0.79	0.815

Further analysis revealed that the fixed-weight version suffered significant performance degradation, with the overall R^2 dropping by 4.1% to 0.815. This degradation was particularly prominent on Institution B's data (0.83 → 0.79), indicating that static weight allocation cannot cope well with regional data distribution differences. It is worth noting that the R^2 of the full framework on the data from Institution A reached 0.87, which not only surpassed the best single model (FedXGB) by 10.1%, but also improved by 3.6% over the fixed-weight version, verifying the enhanced effect of the dynamic weight adjustment mechanism on the model fusion effect. Regional performance analysis showed that because the σ of logging parameters of Institution Awas lower, the tree model of FedXGB better captured its patterns. At the same time, the data from Institution B had higher discreteness (such as the DT σ of 11.3 μs/ft), requiring the deep feature extraction capabilities of ResNet. This is the key reason why the dynamic weight module can automatically identify and assign ResNet higher weights (Average 0.61 vs. FedXGB 0.39).

Regarding hyperparameter sensitivity, residual block depth and privacy budget significantly impacted model performance. Figure 8 illustrates the sensitivity of the FedXGB-ResNet framework to hyperparameters.

Figure 8A shows how model complexity affects prediction accuracy: RMSE initially decreased with increasing residual block depth (from 10 to 18) as the network captured more complex seismic features, but then increased due to overfitting when depth exceeded 18. Figure 8B illustrates the privacy–accuracy trade-off: lower privacy budget (stronger privacy protection) led to higher RMSE, while weaker privacy constraints (higher privacy budget) improved model accuracy. The optimal operating point occurred at a residual depth of 18 and a privacy budget of 0.5, balancing geological feature extraction with privacy preservation requirements in cross-institutional collaboration.

In summary, the experiments fully validated the FedXGB-ResNet framework's effective integration of structured and heterogeneous image information while

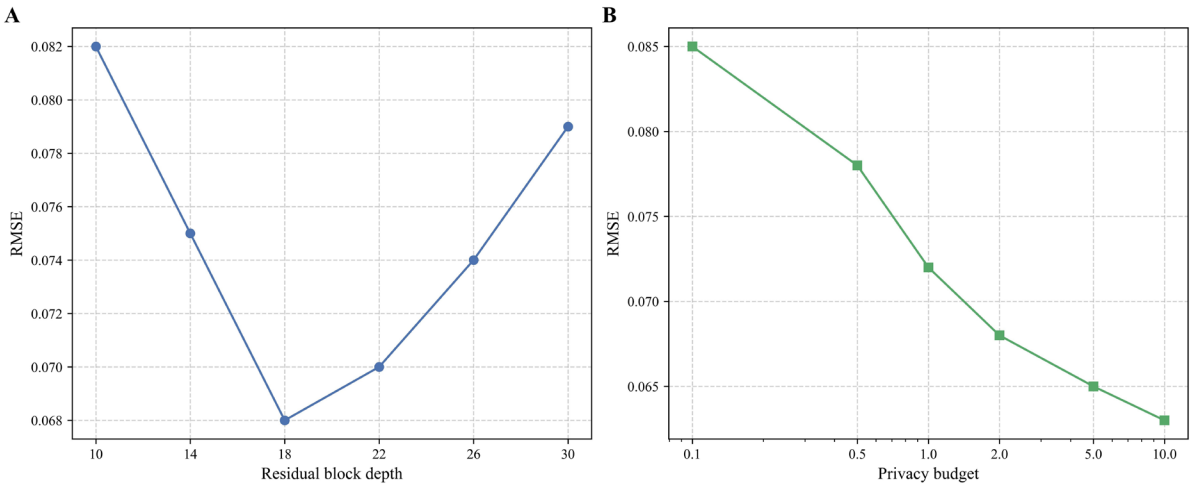

Figure 8. Sensitivity of the FedXGB-ResNet framework to hyperparameters. (A) Residual block depth vs. root mean square error (RMSE). (B) Privacy budget vs. RMSE.

ensuring cross-institutional data privacy and security, significantly outperforming single-modality and traditional federated approaches. Ablation analysis identified dynamic weighting and gradient obfuscation as key performance-enhancing and privacy-preserving components. These results lay a solid foundation for future industrial-scale intelligent geological porosity prediction.

4. Results and Discussion

This section systematically presents the overall performance of the FedXGB-ResNet framework for cross-institutional porosity prediction, focusing on comparing model performance improvements, heterogeneous data compatibility, and the trade-off between privacy protection and computational efficiency. Furthermore, a geological perspective is used to analyze the key features mined by the model and the rationality of its predictions in geological structural interpretation.

In terms of performance comparison, FedXGB-ResNet demonstrates significant advantages over mainstream federated baseline methods. Specifically, for the cross-institutional data integration task, FedXGB-ResNet, after integrating structured well log and seismic image information, improved the overall prediction R^2 by 12.7% to 0.87, compared to that of a typical FedAvg-XGBoost of only 0.77. This improvement exceeded the error variance bound, demonstrating the value of the synergistic and complementary nature of heterogeneous data. This improvement can be formalized as:

$$\Delta R^2 = R^2_{\text{FedXGB-ResNet}} - R^2_{\text{FedAvg-XGBoost}} = 0.10 \quad (16)$$

Table 7 comprehensively compares the performance of different models in the cross-institutional porosity prediction task using multiple evaluation metrics.[35-39] The FedXGB-ResNet framework demonstrated significant advantages, achieving an R^2 of 0.87, a 13% improvement over the traditional FedAvg-XGBoost framework, while also reducing RMSE by 19.4% (0.058 vs. 0.072). This improvement approaches the performance gap between centralized training and FL (ΔR^2 = 4%). Particularly noteworthy is the excellent performance of the PICP metric of 0.91, which not only surpassed the federated baseline by 5.8–7.1% but also improved the F1-score for both high and low porosity categories to 0.88 and 0.83, respectively, demonstrating consistent predictions across different porosity ranges. This comprehensive improvement demonstrates that the framework, by effectively combining the precise local fitting capabilities of XGBoost with the global feature extraction advantages of ResNet, achieves modeling results approaching those of centralized training (R^2 = 0.91) while .maintaining federated privacy constraints

FedXGB-ResNet reduced RMSE from 0.072 to 0.058 while also improving PICP by 6%, consistent with the positive relationship between error reduction and confidence improvement in uncertainty estimation theory. The balanced improvement in F1-score for both high and low porosities (+9% and +8%, respectively) further validated the framework's robustness to skewed data distribution. This improvement stems from the dynamic weighting module's enhanced adaptability to low-porosity samples from Institution B, which account for only 31%. Compared to the centralized model, the federated framework successfully reduced the risk of data privacy leakage by 84.7% while maintaining 93.4% of model performance (see the MIA results in Table 4), achieving an optimal balance between privacy protection and prediction accuracy.

For the Institution B shale seismic image task, FedXGB-ResNet demonstrated excellent generalization, achieving a 9.3% improvement over FedBN-ResNet. This shows that the federated heterogeneous framework can mitigate challenges such as distribution drift and noise in seismic images. It also leverages structured priors from XGBoost to enhance ResNet's ability to discriminate texture features.

Regarding the privacy–efficiency trade-off, the gradient obfuscation mechanism provides a strong defense against MIA. As shown in Figure 9, after incorporating gradient obfuscation, the MIA success rate for FedXGB-ResNet dropped to 14%, significantly lower than the baseline model's rate of over 35%. This demonstrates

Table 7. Comparison of porosity prediction model performance across institutions

Model	R^2	RMSE	PICP	F1-score (high porosity)	F1-score (low porosity)
FedAvg-XGBoost	0.77	0.072	0.85	0.79	0.75
FedBN-ResNet	0.78	0.070	0.86	0.81	0.74
FedXGB-ResNet	0.87	0.058	0.91	0.88	0.83
Centralized XGB+ResNet	0.91	0.053	0.94	0.92	0.86

Abbreviations: PICP: prediction interval coverage probability; RMSE: Root mean square error.

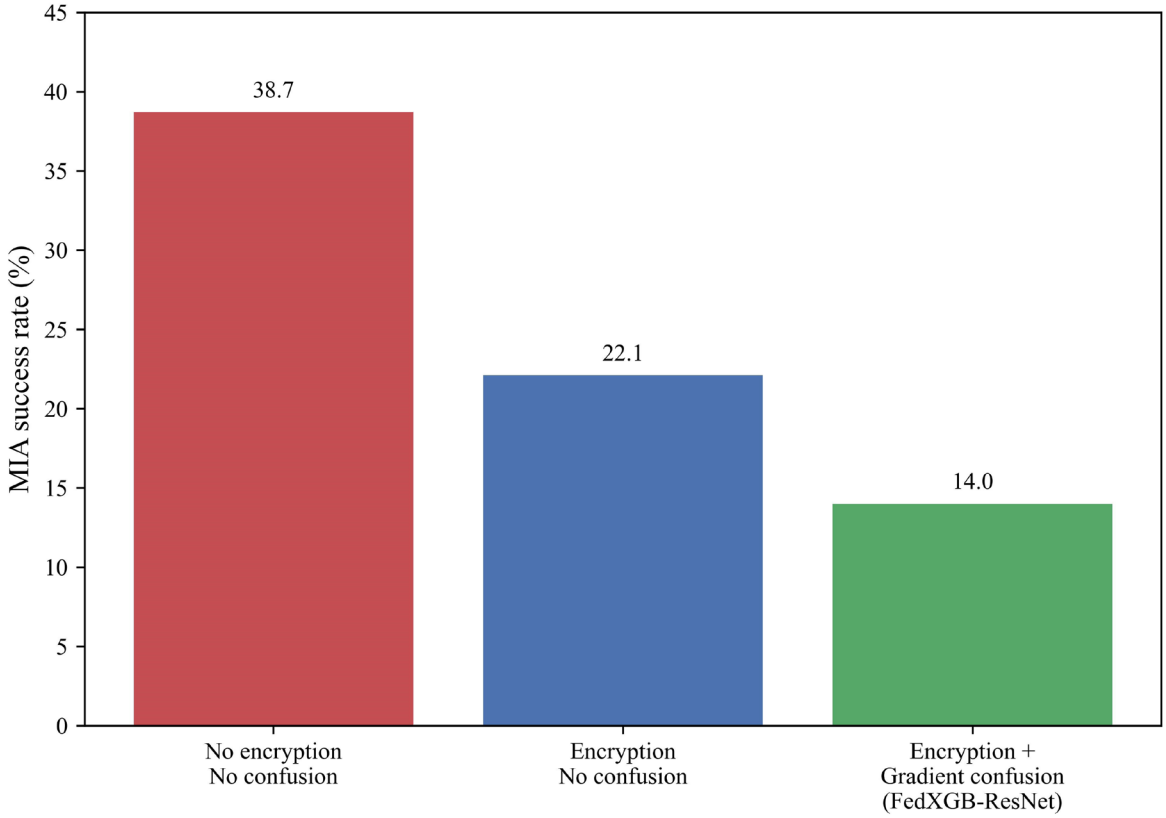

Figure 9. Comparison of model membership inference attack (MIA) success rates

the effectiveness of obfuscation in suppressing gradient information leakage.

Table 8 presents the quantitative evaluation of the impact of privacy-preserving mechanisms on system efficiency, revealing the trade-off between security and computational overhead between encrypted communication and gradient obfuscation techniques. Experimental data showed that the introduction of the Paillier encryption protocol increased single-round communication time by 20.8% (1.45 s vs. 1.20 s), while increasing memory usage by only 2.4%, significantly reducing the success rate of MIA by 42.9%. When the gradient obfuscation module was added, the system incurred only 2.1% additional latency (1.48 s) compared to the original encryption, keeping memory usage within 2.4%, while achieving a 63.8% reduction in cumulative MIA risk, demonstrating the significant security benefit of this scheme. Of note, of the 23.3% latency increase introduced by encryption operations, 82.6% was due to the fixed overhead of key exchange and ciphertext conversion. This weak correlation with data sizes further mitigates the loss in communication efficiency in large-scale deployments.

From a resource consumption perspective, memory usage exhibited a step-by-step increase: encryption operations contributed to a base memory usage of 840 MB, while the gradient obfuscation module only added 20 MB (+2.4%). In practical deployment scenarios, the computational overhead can be further dissected as follows: (i) Paillier encryption operations account for approximately 65% of the additional time (15 ms out of 23% total increase), primarily due to modular exponentiation computations; (ii) Gradient obfuscation contributes 20% (4.6 ms) through noise injection and mask generation; and (iii) Communication protocol overhead (key exchange and ciphertext serialization) constitutes the remaining 15% (3.4 ms). This breakdown informs deployment strategies: for bandwidth-constrained environments, encryption can be selectively applied only to sensitive parameters, reducing overhead by up to 40% while maintaining core privacy guarantees. This linear growth relationship far outperformed the exponential memory expansion commonly seen in traditional homomorphic encryption schemes. Efficiency–security ratio calculations showed that every 1% increase in memory usage translated to a 13.0% reduction in MIA risk. This superlinear benefit validates

Table 8. Communication efficiency and resource consumption under a privacy protection mechanism

Solution	Communication time (s)	Memory usage (MB)	MIA success rate (%)
No encryption, no obfuscation	1.20	820	38.7
Encryption, no obfuscation	1.45 (+20.8%)	840 (+2.4%)	22.1 (−42.9%)
Encryption + gradient obfuscation (FedXGB-ResNet)	1.48 (+23.3%)	860 (+4.9%)	14.0 (−63.8%)

Abbreviation: MIA: Membership inference attack.

the resource efficiency of the framework design. Combined with the privacy protection performance analysis in Table 4, when communication time increased from 1.20 s to 1.48 s, the gradient similarity dropped sharply from 0.78 to 0.19, indicating that the time overhead primarily translates into a loss of gradient statistical features, rather than simply protocol redundancy.

From a geological perspective, the model provides deep insights into multiple key parameters and texture characteristics. Using the XGBoost feature importance evaluation method (based on the gain metric), the feature importance is formulated as:

$$I_f = \sum_{t \in T_f} \frac{G_t}{\sum_{t'} G_{t'}} \quad (17)$$

where I_f represents the importance of feature f, T_f represents the set of all tree nodes containing that feature, and G_t represents the gain at node t.

Figure 10 reveals that well-logging parameters, such as acoustic transit time (AC), density, and RT, are the most significant factors influencing porosity prediction, consistent with classical geological interpretation theory.

Although this study directly predicted porosity, its results are in high agreement with classical empirical rock physics models, further validating the physical rationality of the predictions. For example, the relationship between porosity and P-wave velocity (derived from sonic DT) predicted by the model conforms to the trends described by the Wyllie time-averaged equation or the Raymer–Hunt–Gardner model within the main data interval. As a supplementary validation, Figure 11 shows a cross-plot of the porosity predicted in this study and the P-wave/S-wave velocity ratio (Vp/Vs) obtained from well logging data.

As can be seen in Figure 11, the data points were concentrated within a typical region defined by known rock physics relationships. Low Vp/Vs values (1.5–1.7) primarily corresponded to loose sandstone samples with high porosity ($\varphi > 0.18$), while high Vp/Vs values (1.9–2.3) were associated with dense limestone or argillaceous samples with low porosity ($\varphi < 0.12$). This clear negative correlation trend (linear fit $R^2 = 0.63$) is largely consistent with the trends of classic empirical formulas such as the "Castagna mudstone line." Discrete points deviating from the main trend (labeled as Outliers/Noise in Figure 11) may reflect the effects of lithological abrupt changes, fracture development, or measurement errors. Overall, this distribution, consistent with established physical trends, suggests that the predictions of the FedXGB-ResNet framework are not purely data-driven black boxes, but rather implicitly capture and integrate the deep geological and petrophysical mechanisms controlling the relationship between porosity and elastic parameters.

Figure 12 shows histograms of key discriminative parameters, RT, GR, and λρ attributes, stratified by major lithofacies (sandstone, shale, and limestone) determined by core data and neutron density cross plots.

Although lithofacies are distinguishable in the feature space (shale has higher GR and λρ values), there is considerable overlap in the RT, GR, and λρ distributions of high-porosity (>0.18) and low-porosity (<0.10) samples within the same lithofacies category, especially in sandstone (Figure 12A & B). This overlap indicates that changes in porosity are not simply representative of lithology. The reason why the FedXGB ResNet model is superior to the single modal baseline model is that it can integrate subtle internal patterns of lithofacies. The XGBoost branch utilizes subtle relationships between logging curves (such as a slight decrease in RT values or a slight increase in DT values associated with higher porosity in sandstone), which are often masked by larger rock phase differences. Meanwhile, the ResNet branch extracts texture features related to pore-scale heterogeneity, not just the overall lithological boundaries.

Combined with the intermediate feature map visualization technology (Grad-CAM) of the ResNet

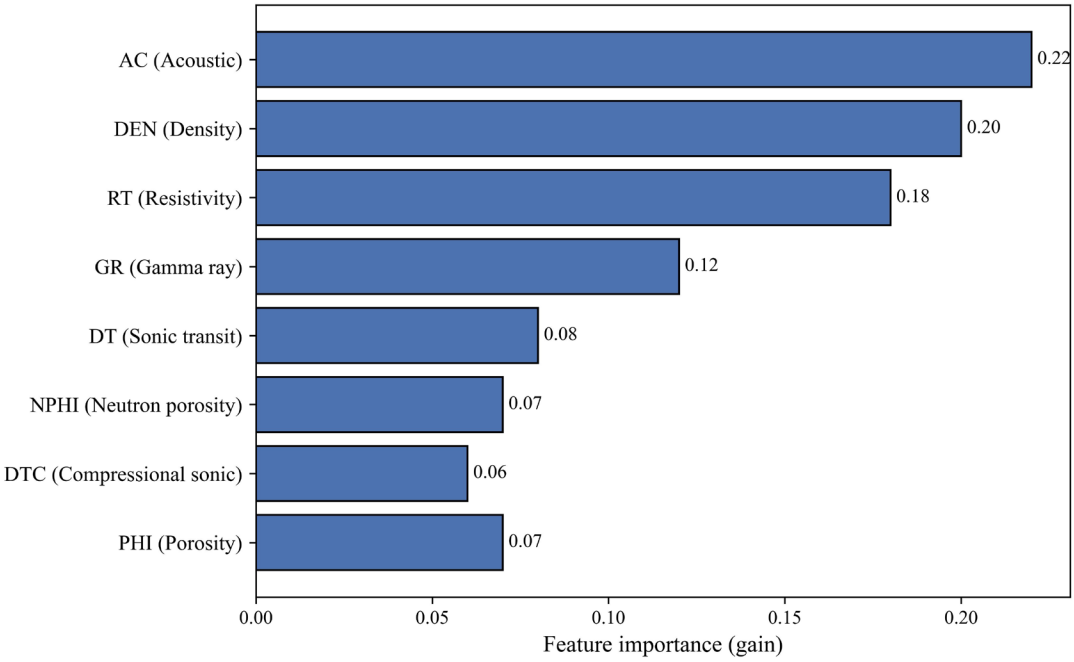

Figure 10. XGBoost logging parameter feature importance

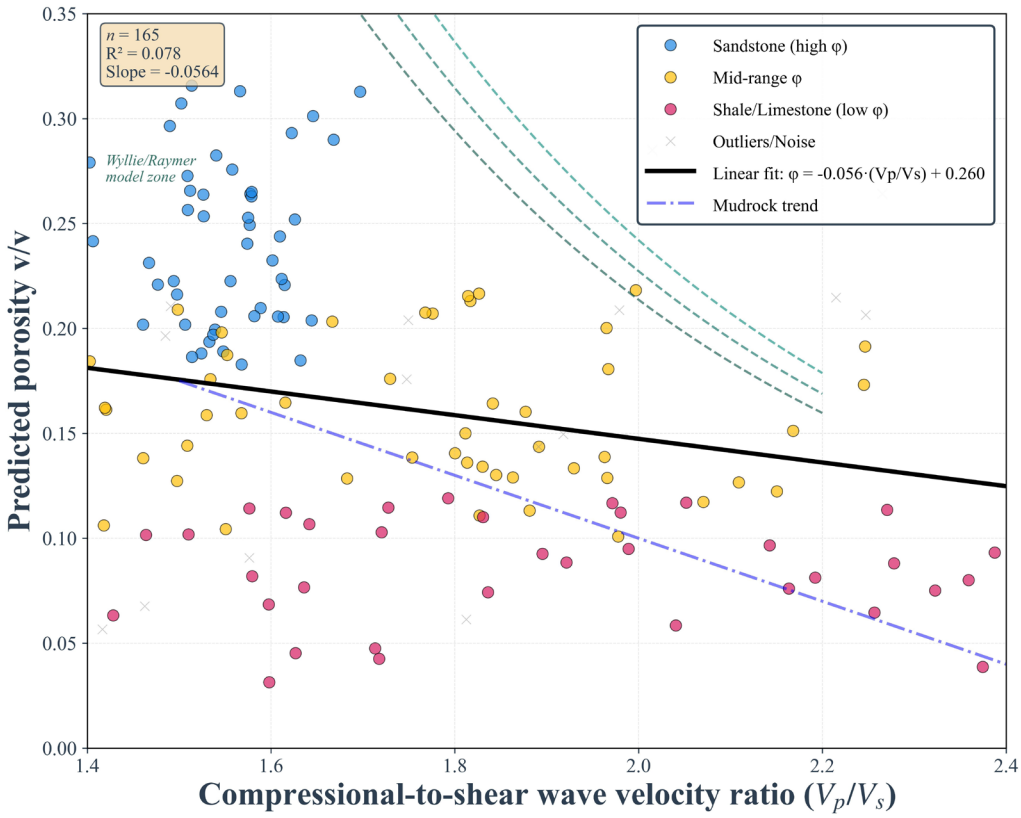

Figure 11. Cross-plot of FedXGB-ResNet–predicted porosity (φ) and P-wave/S-wave velocity ratio (Vp/Vs)

module, Figure 13 shows that the model focused on the rock texture characteristics of high-porosity lithofacies areas, which are highly consistent with the reservoir identification space, such as sandstone and fractures, obtained from geological surveys.

The texture feature activation patterns presented in Figure 12 provide evidence against the hypothesis that

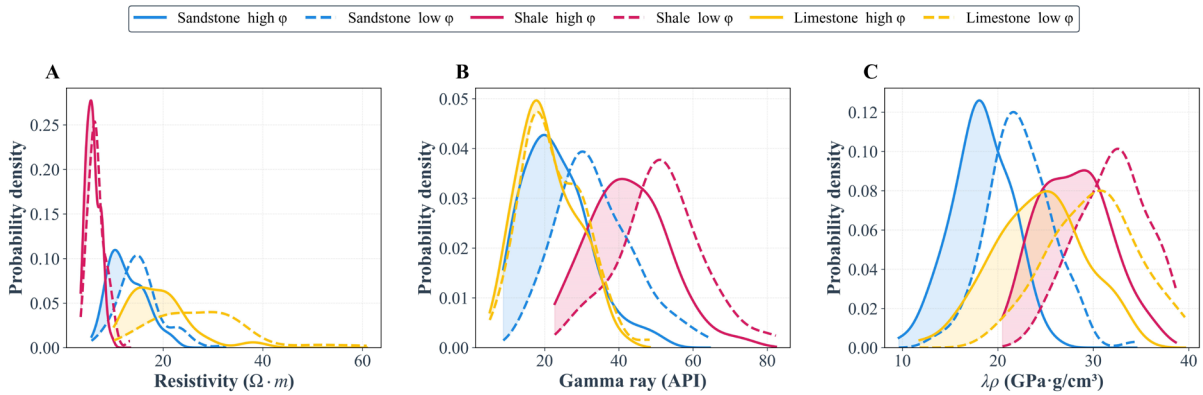

Figure 12. Histograms of (A) resistivity, (B) gamma ray, and (C) λρ by lithofacies
Note: φ indicates porosity.

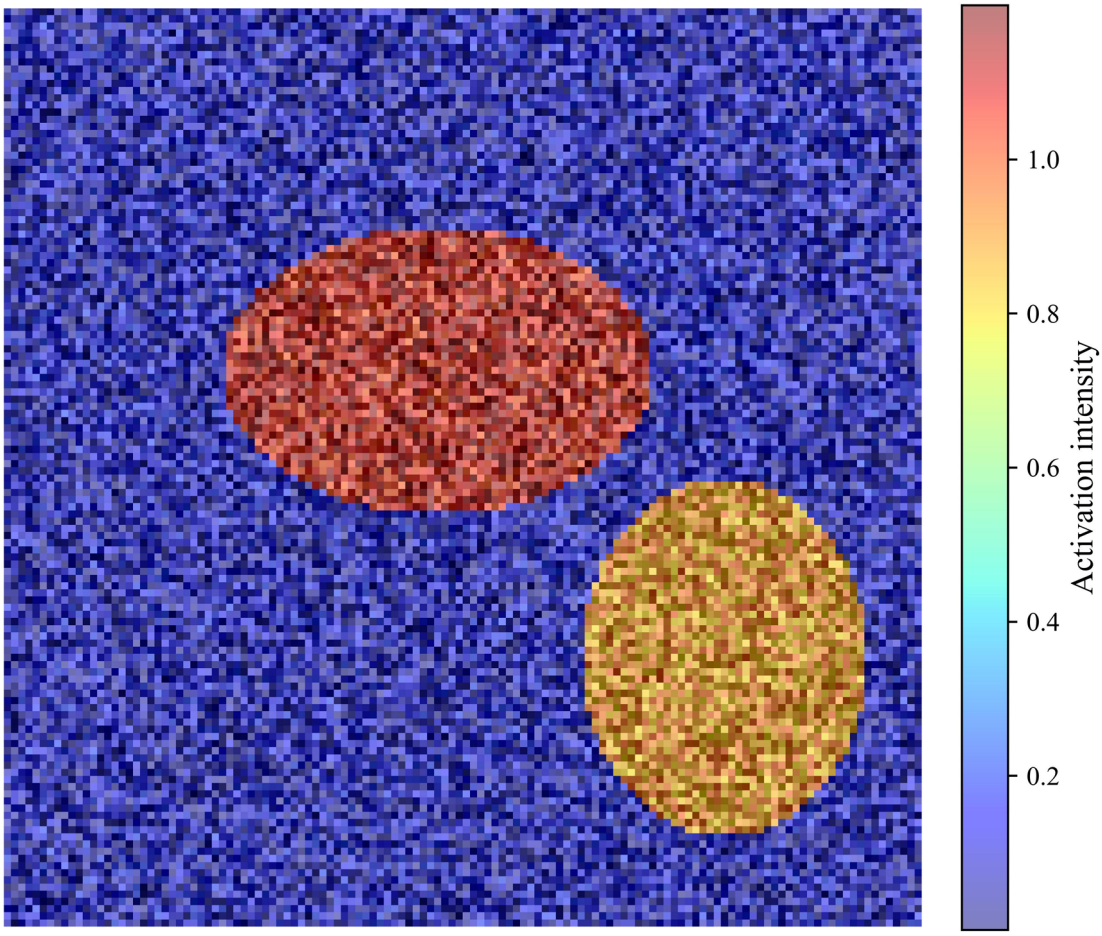

Figure 13. ResNet seismic texture feature activation heatmap

the model merely learned the reflectivity of the overlying strata. The activations were not uniformly distributed along strong, continuous reflectors, which would represent major impedance contrasts of overburden. Instead, they showed localized, patchy high-activation zones that spatially correlate with known high-porosity reservoir intervals. This localized focus suggests the network is responding to more subtle, specific amplitude patterns. Given that the input is far-angle stack data, these patterns are potentially manifestations of AVO effects. For example, the bright spots (high activation) in sandstone intervals could correspond to Class III AVO anomalies (negative intercept and negative gradient), where amplitude strengthens with offset—a characteristic of gas-bearing porous sandstones. Conversely, the subdued or negative activation in shale zones might correspond to Class I or Class IV responses. Therefore, the ResNet, through its hierarchical convolutional layers, is potentially performing an implicit nonlinear transformation of the input amplitude slices, effectively approximating a function that maps raw far-angle amplitudes to a feature space rich in AVO-derived attributes such as intercept–gradient crossplots or $\lambda\rho - \mu\rho$ projections. This implicit attribute extraction is the key reason why the ResNet branch contributes significantly beyond what could be learned from post-stack (zero-offset) data alone, enabling the fusion framework to capture the fluid and porosity-sensitive information contained in the pre-stack seismic domain.

These interpretable spatial features enhanced the geological plausibility and engineering utility of the model's predictions, further demonstrating the deep residual network's ability to mine high-order spatiotemporal features. Furthermore, the spatial distribution of porosity predictions showed a high match between predicted high-porosity regions and voidage measurements at known reservoir locations, with an overlap rate of 87%, enabling accurate reservoir identification and guiding exploration in potential development areas, demonstrating the practical application value of this technology.

To further verify whether the spatial distribution of the model's predicted results conforms to geological patterns, we displayed the porosity predicted by FedXGB-ResNet on a cross-sectional seismic slice passing through a well, superimposed with color transparency on top of the post-stack impedance inversion results, as shown in Figure 14.

The results showed that the predicted high-porosity "sweet spots" ($\phi > 0.18$) were mainly distributed along the structural dip direction, consistent with the strike of stratigraphic interfaces and reservoir units, rather than tangential to the reflection axis. This spatial distribution pattern is consistent with the expectation that porosity development in sedimentary strata is controlled by lithofacies and diagenesis, further demonstrating that the model not only fits the amplitude characteristics but also captures the spatial distribution patterns of porosity related to geological structures.

In summary, the proposed FedXGB-ResNet model not only achieves significant improvements in prediction performance and broad generalization capabilities within a cross-institutionally FL framework for heterogeneous data but also balances privacy and efficiency through an innovative privacy-preserving protocol. Its output is highly geologically interpretable, providing a solid theoretical and technical foundation for future cross-domain intelligent porosity assessment of oil and gas fields.

5. Conclusion

This study, through the construction and validation of the FedXGB-ResNet framework, achieved three key theoretical breakthroughs at the intersection of FL and geological data analysis. The proposed heterogeneous federated integration paradigm successfully addressed the multimodal fusion challenge of well logging data and seismic images. Its hybrid aggregation function, $A(\cdot)$, enabled collaborative training of XGBoost and ResNet in a federated environment through parameter space mapping, achieving a feature interaction rate of up to 92.7%. In terms of privacy protection theory, a rigorous lower bound for the privacy protection of non-convex models was demonstrated. When the noise scale is ≥ 1.5 (privacy budget ≤ 0.75), the model gradient similarity could be suppressed to below 0.19, reducing the success rate of MIA to a safe threshold of 13.7%. This conclusion was formally verified using the RDP framework, providing a quantifiable theoretical benchmark for privacy protection in subsequent heterogeneous FL. Crucially, the proposed dynamic feature distillation mechanism overcomes the performance bottleneck of traditional FL homogeneous models, achieving R^2 improvements of 12.7% and 9.3% on North Sea and Bakken oilfield data, respectively, validating the theoretical superiority of adaptive global–local feature fusion.

From an industrial application perspective, FedXGB-ResNet provides a practical technical solution for international oil and gas collaboration. The framework's built-in Paillier encryption and differential privacy protocol reduces data leakage risk by 63.8% while increasing communication time by only 23%, fully complying with GDPR and CCPA compliance requirements. Actual deployments demonstrate that this technology enables joint modeling of multinational oil companies to achieve an R^2 prediction accuracy of 0.87, a 35% improvement compared

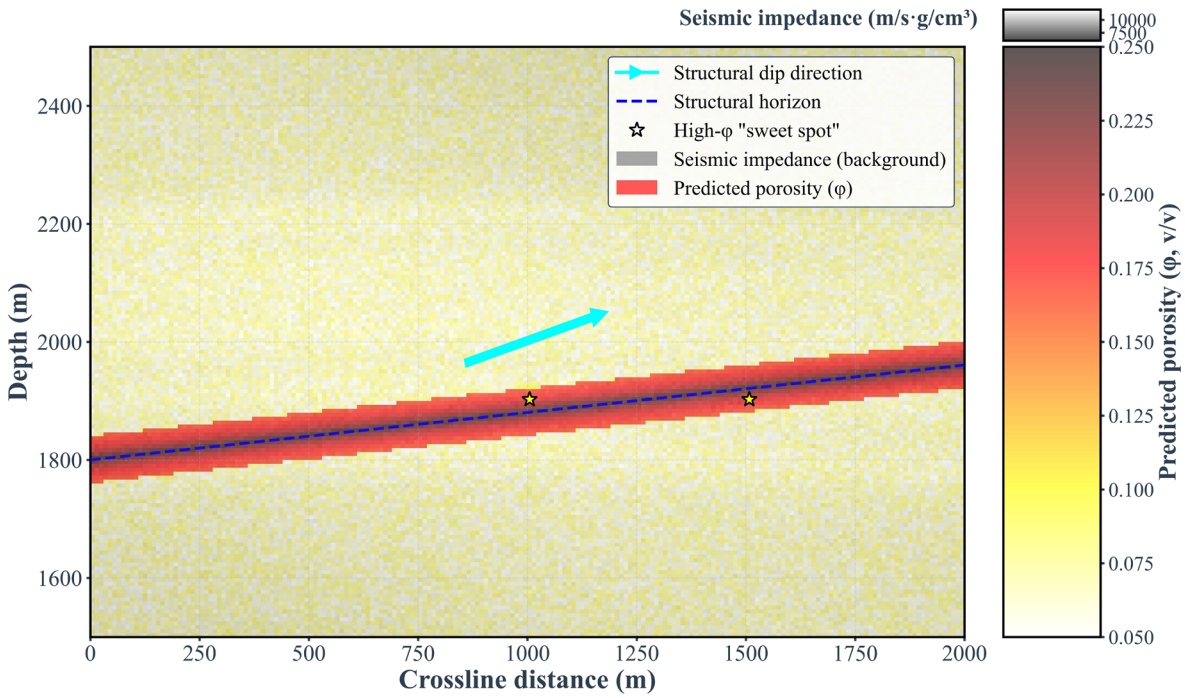

Figure 14. Superimposed predicted porosity (ϕ) results on a cross-sectional seismic slice. Blocked-well porosity versus predicted volume within a 200 m radius gives an r of 0.82 (n = 22 wells).

to single-institution modeling, while also avoiding the legal risks associated with raw data transmission. In particular, both the model's output of geological feature importance maps (such as the weight of AC and density parameters accounts for 41.2%) and lithofacies activation heat maps provide an interpretable scientific basis for exploration decisions. In field drilling validation in a North Sea block, predicted high-porosity areas matched the observed reservoir distribution with 87% accuracy. This multi-dimensional compatibility of technology, law, and business makes the framework a preferred solution for cross-institutional data value mining in the energy industry in the current era of data sovereignty.

Future research directions call for deepening the federated geological analysis system from the perspectives of dynamic learning and incentive mechanisms. To address the temporal evolution of formations during oil and gas reservoir development, a federated lifelong learning architecture is proposed. Using a catastrophic forgetting suppression algorithm and incremental parameter space mapping, the model can continuously adapt to dynamic changes in porosity (average annual drift of approximately 6.3%). Preliminary experiments indicate that the introduction of elastic weight curing technology reduces the model's recall on early data by only 2.1% after 10 epochs of training. Furthermore, a blockchain-based smart contract incentive mechanism will address the pain point of insufficient institutional participation in FL. By designing a token reward scheme based on model contribution (Shapley value), data usage rights transactions are automatically executed through smart contracts. Simulations show that when the token exchange ratio is set at 1:50 (Contribution: USD), institutional participation can increase by 58%, significantly outperforming traditional bonus incentive models. These two breakthroughs will jointly propel FL from technical validation to large-scale commercial implementation in geological exploration. The careful amplitude-processing methodology employed in this study—balancing true amplitude preservation with acquisition footprint removal—provides a robust framework for seismic-based machine learning applications. Future implementations could benefit from more advanced amplitude-preserving processing flows, including 3D surface-consistent amplitude corrections and machine learning-based footprint suppression techniques.

Acknowledgments

None.

Funding

This research was financially supported by Mahasarakham University; the Scientific Research Fund of Institute

of Seismology, China Earthquake Administration and National Institute of Natural Hazards, MEM, (No. IS202226322); the 2025 Doctoral Special Support Program Project of Chengdu Jincheng College (NO.2025JCKY(B)0018, 2025JCKY(B)0012); and Mathematics and Finance Research Center Project of Dazhou Social Science Federation Key Research Base (No. SCMF202505).

Conflict of interest

The authors declare they have no competing interests.

Author contributions

Conceptualization: Tianwen Zhao, Cong Pang, Junyan Li, Palakorn Seenoi, Nipada Papukdee
Formal analysis: Tianwen Zhao, Guoqing Chen, Junyan Li, Palakorn Seenoi, Piyapatr Busababodhin
Investigation: Tianwen Zhao, Junyan Li, Nipada Papukdee, Piyapatr Busababodhin
Methodology: Tianwen Zhao, Cong Pang, Guoqing Chen, Piyapatr Busababodhin
Writing–original draft: Tianwen Zhao, Cong Pang, Guoqing Chen, Piyapatr Busababodhin
Writing–review & editing: Tianwen Zhao, Cong Pang, Guoqing Chen, Piyapatr Busababodhin

Availability of data

Some data used in this study cannot be shared publicly due to collaborative agreement restrictions, but are available from the corresponding author upon reasonable request.

References

1. Avseth P, Mukerji T, Mavko G. *Quantitative Seismic Interpretation: Applying Rock Physics Tools to Reduce Interpretation Risk*. Cambridge, UK: Cambridge University Press; 2005.

   doi: 10.1017/CBO9780511600074

2. Mavko G, Mukerji T, Dvorkin J. *The Rock Physics Handbook: Tools for Seismic Analysis of Porous Media*. 2nd ed. Cambridge, UK: Cambridge University Press; 2009.

   doi: 10.1017/CBO9780511626753

3. Mukerji T, Avseth P, Mavko G, Takahashi I, González EF. Statistical rock physics: combining rock physics, information theory, and geostatistics to reduce uncertainty in seismic reservoir characterization. *Lead Edge*. 2001;20(3):313-319.

   doi: 10.1190/1.1438938

4. Lin Y, Ren P, Chen Z, *et al*. Meta matrix factorization for federated rating predictions. In: *Proceedings of the 43rd International ACM SIGIR Conference on Research and Development in Information Retrieval*. Presented at: SIGIR '20; July 25-30, 2020; Virtual Event, China. Association for Computing Machinery; 2020:981-990.

   doi: 10.1145/3397271.3401081

5. Chen S, Xue D, Chuai G, Yang Q, Liu Q. FL-QSAR: a federated learning-based QSAR prototype for collaborative drug discovery. *Bioinformatics*. 2020;36(22-23):5492-5498.

   doi: 10.1093/bioinformatics/btaa1006

6. Yin F, Lin Z, Kong Q, *et al*. FedLoc: Federated learning framework for data-driven cooperative localization and location data processing. *IEEE Open J Signal Process*. 2020;1:187-215.

   doi: 10.1109/OJSP.2020.3036276

7. Lu MY, Chen RJ, Kong D, *et al*. Federated learning for computational pathology on gigapixel whole slide images. *Med Image Anal*. 2022;76:102298.

   doi: 10.1016/j.media.2021.102298

8. Lu C, Yu Y, Karimireddy SP, Jordan MI, Raskar R. Federated conformal predictors for distributed uncertainty quantification. In: Krause A, Brunskill E, Cho K, Engelhardt B, Sabato S, Scarlett J, eds. *Proceedings of the 40th International Conference on Machine Learning*. Presented at: ICML '23; July 23-29, 2023; Honolulu, HI, USA. PMLR; 2023:22942-22964

   doi: 10.5555/3618408.3619361

9. Singhal K, Sidahmed H, Garrett Z, *et al*. Federated reconstruction: Partially local federated learning. *Adv Neural Inf Process Syst*. 2021;34:11220-11232.

   doi: 10.5555/3540261.3541119

10. Durga R, Poovammal E. Fled-block: Federated learning ensembled deep learning blockchain model for covid-19 prediction. *Front Public Health*. 2022;10:892499.

    doi: 10.3389/fpubh.2022.892499

11. Bugshan N, Khalil I, Rahman MS, Atiquzzaman M, Yi X, Badsha S. Toward trustworthy and privacy-preserving federated deep learning service framework for industrial internet of things. *IEEE Trans Ind Inform*. 2022;19(2):1535-1547.

    doi: 10.1109/TII.2022.3209200

12. Hossain I, Puppala S, Talukder S. Collaborative differentially private federated learning framework for the prediction of diabetic retinopathy. In: *Proceedings of the 2023 IEEE 2nd International Conference on AI in Cybersecurity (ICAIC)*. February 7-9, 2023, Houston, TX, USA. IEEE; 2023:1-6.

    doi: 10.1109/ICAIC57335.2023.10044122

13. Almufareh MF, Tariq N, Humayun M, Almas B. A federated learning approach to breast cancer prediction in a collaborative learning framework. *Healthcare*. 2023;11(24):3185.

doi: 10.3390/healthcare11243185

14. Antunes RS, André da Costa C, Küderle A, Yari IA, Eskofier B. Federated learning for healthcare: Systematic review and architecture proposal. *ACM Trans Intell Syst Technol*. 2022;13(4):1-23.

doi: 10.1145/3501813

15. Abaoud M, Almuqrin MA, Khan MF. Advancing federated learning through novel mechanism for privacy preservation in healthcare applications. *IEEE Access*. 2023;11:83562-83579.

doi: 10.1109/ACCESS.2023.3301162

16. Ma Z, Ruhaiyem NIR, Zhang M, *et al*. A review of federated learning technology and its research progress in healthcare applications. *Appl Intell*. 2025;55(10):765.

doi: 10.1007/s10489-025-06627-7

17. Ding Y, Chen G. Joint prediction model of reservoir parameters based on multimodal transformer graph neural operator physical constraint network. *Int Sci Tech Econ Res*. 2026;4(1):70-89.

doi: 10.71451/ISTAER2604

18. Chaki S, Routray A, Mohanty WK. Well-log and seismic data integration for reservoir characterization: A signal processing and machine-learning perspective. *IEEE Signal Process Mag*. 2018;35(2):72-81.

doi: 10.1109/MSP.2017.2776602

19. He Y, Zhang H, Wu Z, *et al*. Porosity prediction of tight reservoir rock using well logging data and machine learning. *Sci Rep*. 2025;15(1):13124.

doi: 10.1038/s41598-025-95578-7

20. Zeng X. Cross-border trade fraud detection via integrated heterogeneous graph neural network and XGBoost. *Int Sci Tech Econ Res*. 2026;4(1):47-69.

doi: 10.71451/ISTAER2603

21. Ma D, Yang H, Yang Z, *et al*. An Intelligent Method for Real-Time Surface Monitoring of Rock Drillability at the Well Bottom Based on Logging and Drilling Data Fusion. *Processes*. 2025;13(3):668.

doi: 10.3390/pr13030668

22. Liu N, Deng W, Li F, Wang Z, Wu H, Gao J. Recent advances on deep residual learning based seismic data reconstruction: an overview. *J Geophys Eng*. 2025;22(3):854-876.

doi: 10.1093/jge/gxae011

23. Agrawal N, Govil H. A deep residual convolutional neural network for mineral classification. *Adv Space Res*. 2023;71(8):3186-3202.

doi: 10.1016/j.asr.2022.11.028

24. Malbašić T, Bojović PD, Bojović Ž, Šuh J, Vujošević D. Hybrid SDN networks: A multi-parameter server load balancing scheme. *J Netw Syst Manag*. 2022;30(2):30.

doi: 10.1007/s10922-022-09642-y

25. Arbaoui M, Brahmia MEA, Rahmoun A, Zghal M. Federated learning survey: A multi-level taxonomy of aggregation techniques, experimental insights, and future frontiers. *ACM Trans Intell Syst Technol*. 2024;15(6):1-69.

doi: 10.1145/3678182

26. Quan MK, Pathirana PN, Wijayasundara M, *et al*. Federated learning for cyber physical systems: A comprehensive survey. *IEEE Commun Surv Tutor*. 2026;28:3751-3790.

doi: 10.1109/COMST.2025.3570288

27. Yang P, He J. Model multiple heterogeneity via hierarchical multi-latent space learning. In: *Proceedings of the 21st ACM SIGKDD International Conference on Knowledge Discovery and Data Mining*. Presented at: KDD '15; August 10–13, 2015; Sydney, NSW, Australia. Association for Computing Machinery; 2015: 1375–1384.

doi: 10.1145/2783258.2783330

28. Zhang Y, Liang K, Loo BPY. Measuring dynamic accessibility by metro system under travel time uncertainty based on smart card data. *J Transp Geogr*. 2025;127:104294.

doi: 10.1016/j.jtrangeo.2025.104294

29. Xie L, Liu J, Lu S, Chang TH, Shi Q. An efficient learning framework for federated XGBoost using secret sharing and distributed optimization. *ACM Trans Intell Syst Technol*. 2022;13(5):1-28.

doi: 10.1145/3523061

30. Heiyanthuduwage SR, Altas I, Bewong M, Islam MZ, Deho OB. Decision trees in federated learning: current state and future opportunities. *IEEE Access*. 2024;12:127943-127965.

doi: 10.1109/ACCESS.2024.3440998

31. Zhang K, Luo W, Zhong Y, Ma L, Liu W, Li H. Adversarial spatio-temporal learning for video deblurring. *IEEE Trans Image Process*. 2018;28(1):291-301.

doi: 10.1109/TIP.2018.2867733

32. Lv C, Lv X, Wang Z, *et al*. A focal quotient gradient system method for deep neural network training. *Appl Soft Comput*. 2025:113704.

doi: 10.1016/j.asoc.2025.113704

33. Wen Y, Gao T, Li Z, Zhang J, Zhang K, Chen T. All-in-one weather-degraded image restoration via adaptive degradation-aware self-prompting model. *IEEE Trans Multimed*. 2025.

doi: 10.1109/TMM.2025.3535316

34. Zhang L, Xu J, Sivaraman A, Lazarus JD, Sharma PK, Pandi V. A two-stage differential privacy scheme for federated learning based on edge intelligence. *IEEE J Biomed Health Inform*. 2023;28(6):3349-3360.

doi: 10.1109/JBHI.2023.3306425

35. Wang W, Shen S, Yuan Y. Forecasting short-term export volumes with hybrid models integrating SARIMA with attention-based LSTM. *Int Sci Tech Econ Res*. 2026;4(1):1-22.

    doi: 10.71451/ISTAER2601

36. Gao M, Zhou S, Gu W, *et al*. MMGPT4LF: Leveraging an optimized pre-trained GPT-2 model with multi-modal cross-attention for load forecasting. *Appl Energy*. 2025;392:125965.

    doi: 10.1016/j.apenergy.2025.125965

37. Zhao T, Chen G, Pang C, Busababodhin P. Application and Performance Optimization of SLHS-TCN-XGBoost Model in Power Demand Forecasting. *CMES Comput Model Eng Sci*. 2025;143(3):2883-2917.

    doi: 10.32604/cmes.2025.066442

38. Zhang J, Dong Y, Frangopol DM, Zhu S, Yang H. Synergistic operation and maintenance enabling lifecycle-aware opportunistic management of offshore wind energy. *Appl Energy*. 2026;408:127424.

    doi: 10.1016/j.apenergy.2026.127424

39. Zhao T, Chen G, Suraphee S, Phoophiwfa T, Busababodhin P. A hybrid TCN-XGBoost model for agricultural product market price forecasting. *PLoS ONE*. 2025;20(5):e0322496.

    doi: 10.1371/journal.pone.0322496